

# Enabling automated magnetic resonance imaging-based targeting assessment during dipole field navigation

Maxime Latulippe,<sup>1</sup> Ouajdi Felfoul,<sup>2</sup> Pierre E. Dupont,<sup>2</sup> and Sylvain Martel<sup>1,a)</sup>

<sup>1</sup>Department of Computer and Software Engineering, Institute of Biomedical Engineering, Polytechnique Montréal, Québec H3T 1J4, Canada

<sup>2</sup>Department of Cardiac Surgery, Boston Children's Hospital, Harvard Medical School, Boston, Massachusetts 02115, USA

(Received 18 November 2015; accepted 2 February 2016; published online 12 February 2016)

The magnetic navigation of drugs in the vascular network promises to increase the efficacy and reduce the secondary toxicity of cancer treatments by targeting tumors directly. Recently, dipole field navigation (DFN) was proposed as the first method achieving both high field and high navigation gradient strengths for whole-body interventions in deep tissues. This is achieved by introducing large ferromagnetic cores around the patient inside a magnetic resonance imaging (MRI) scanner. However, doing so distorts the static field inside the scanner, which prevents imaging during the intervention. This limitation constrains DFN to open-loop navigation, thus exposing the risk of a harmful toxicity in case of a navigation failure. Here, we are interested in periodically assessing drug targeting efficiency using MRI even in the presence of a core. We demonstrate, using a clinical scanner, that it is in fact possible to acquire, in specific regions around a core, images of sufficient quality to perform this task. We show that the core can be moved inside the scanner to a position minimizing the distortion effect in the region of interest for imaging. Moving the core can be done automatically using the gradient coils of the scanner, which then also enables the core to be repositioned to perform navigation to additional targets. The feasibility and potential of the approach are validated in an *in vitro* experiment demonstrating navigation and assessment at two targets. © 2016 AIP Publishing LLC. [<http://dx.doi.org/10.1063/1.4941925>]

Controlled magnetic navigation of therapeutic carriers inside blood vessels is a promising technology for targeted drug delivery.<sup>1,2</sup> By combining a drug with superparamagnetic nanoparticles, these carriers, if magnetized by an external magnetic field, can be steered via forces induced by magnetic gradients. To maximize the resulting forces, the magnetizing field must be strong enough to bring the particles to saturation magnetization. One approach is magnetic resonance targeting (MRT) which exploits the strong static field of a magnetic resonance imaging (MRI) scanner and uses the gradient coils of the scanner to cause systemically circulating magnetized particles to accumulate at a desired location in the body.<sup>3</sup> Because superparamagnetic particles act as MRI contrast agents, MRT also provides the capability to assess particle accumulation. An alternative approach, explored in this paper, is to steer the particles along a predefined vascular route, from an injection point directly toward the targeted tumor, and thus minimize the toxicity and inefficiency of systemic circulation. Although the behavior of carriers is predictable, such navigation is ideally performed with closed-loop control in order to compensate for the uncertainties of the real-world vascular environment. This has been achieved with magnetic resonance navigation (MRN),<sup>4</sup> which also uses an MRI scanner and enables real-time tracking of particles during the navigation process<sup>5</sup> using a specific imaging sequence such as MS-SET.<sup>6</sup> Considering the very small magnetic volume of the therapeutic carriers (e.g., max. 300  $\mu\text{m}$  in size for liver chemoembolization), the capabilities of MRN in

high blood flow velocities found in human arteries are, however, limited by the relatively weak gradients achievable with conventional clinical MRI scanners (typically 40 mT/m). While balloon catheters can be used to reduce the vascular flow rate, this approach translates to longer required intervention times. Electromagnetic actuation systems<sup>7-9</sup> can generate much higher gradients ( $>300$  mT/m), but lack the required field strength to saturate the particles. The only method so far that combines a high magnetizing field with high gradient strengths ( $>300$  mT/m) for whole-body interventions in deep tissues is dipole field navigation (DFN).<sup>10</sup> This method consists in inserting large ferromagnetic cores around the patient inside an MRI scanner to generate very strong gradients. However, the resulting distortion of the static field in the scanner prevents imaging. Indeed, MRI traditionally requires a homogeneous field for proper image reconstruction, and inhomogeneities can introduce imaging artifacts which affect the accuracy of anatomical details. Various approaches and algorithms have been developed to compensate for normal field inhomogeneities found in the MRI environment.<sup>11</sup> In particular, special imaging sequences have been shown to be more robust to field inhomogeneities and improve the image quality around metal implants.<sup>12,13</sup> None of these methods, however, can cope with the much stronger and unusual field distortion caused by the ferromagnetic cores in DFN. As such, DFN has been limited to open-loop navigation and has relied on the accuracy of magnetic models and precise core positioning to achieve targeting accuracy. To ensure accurate targeting and to avoid potential morbidities from inaccurate targeting, drug delivery should be at least periodically

<sup>a)</sup>Electronic mail: [sylvain.martel@polymtl.ca](mailto:sylvain.martel@polymtl.ca).

assessed during an intervention so that core positions can be adjusted as necessary. Ideally, such an informed open-loop scheme would be achieved automatically and without retracting the cores from the scanner to speed up the intervention.

In this letter, we identify specific angular regions around a ferromagnetic core where imaging artifacts are minimized and exploit these regions for assessing targeting efficiency. Furthermore, using the imaging gradient coils as a propulsion mechanism,<sup>4,14</sup> we show that the core can be moved automatically between positions optimized for navigation and for imaging (see Fig. 1).

In DFN, both the nanoparticles and the cores are assumed to be magnetized at saturation by the static field  $\mathbf{B}_0$  of the MRI scanner. The strong magnetic gradients result from the distortion of  $\mathbf{B}_0$  around the cores and induce magnetic forces on the particles according to

$$\mathbf{F}_{mag} = \nabla(\mathbf{m}_p \cdot \mathbf{B}), \quad (1)$$

where  $\mathbf{m}_p$  is the magnetic moment of a particle and  $\mathbf{B} = \mathbf{B}_0 + \mathbf{B}_{core}$  is the total field experienced by the particle. For a single spherical core of radius  $R$ , volume  $V$ , saturation magnetization  $\mathbf{M}_{sat}$ , and magnetic moment  $\mathbf{m} = V\mathbf{M}_{sat}$

$$\mathbf{B}_{core}(r > R) = \frac{\mu_0}{4\pi} \left[ 3 \frac{(\mathbf{m} \cdot \mathbf{r})\mathbf{r}}{r^5} - \frac{\mathbf{m}}{r^3} \right], \quad (2)$$

where  $\mathbf{r}$  is the position vector relative to the core's center,  $r = \|\mathbf{r}\|$ , and  $\mu_0 = 4\pi \times 10^{-7}$  H/m is the vacuum permeability. Fundamentally in MRI, this non-uniform field added to  $\mathbf{B}_0$  results in a position-dependent offset of the Larmor frequency  $f = \frac{\gamma}{2\pi} B$  of the nucleus used for resonance signal acquisition, where  $\gamma$  is the gyromagnetic ratio of the nucleus. As shown in Fig. 2 for a chrome steel core ( $M_{sat} = 1.4 \times 10^6$  A/m) and the hydrogen nucleus ( $\gamma = 42.576$  MHz/T), this offset varies non-linearly around the core and reaches zero at four location angles. Assuming that the core is magnetized in the  $z$ -axis direction (i.e.,  $\mathbf{B}_0 = B\hat{z}$ ), the total field strength in the far field of the core can be approximated as

$$B \approx B_z = B_0 + \frac{\mu_0 m}{4\pi r^5} (3z^2 - r^2), \quad (3)$$

$$= B_0 + \frac{\mu_0 m}{4\pi r^3} (3 \cos^2 \theta - 1), \quad (4)$$

where  $\theta$  is the angle between the position vector  $\mathbf{r}$  and  $\mathbf{B}_0$ . For a chrome steel core in a 3 T field, this approximation yields an error below 0.1% at  $\sim 2R$  from the core's center. From Eq. (4), which was obtained by substituting  $z = r \cos \theta$ , the contribution of the core to the total field is minimized when

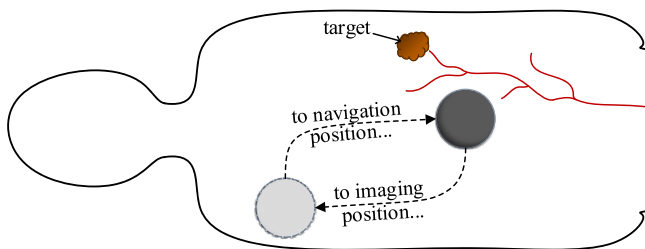


FIG. 1. To assess targeting in DFN, the core can be moved between locations optimized for navigation and for imaging.

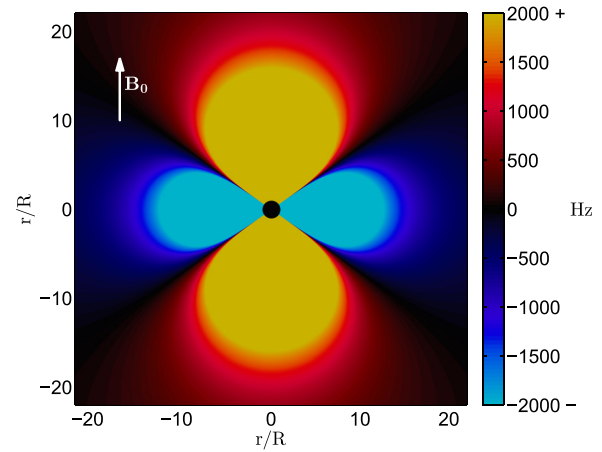


FIG. 2. Simulated offset of the Larmor frequency of hydrogen around a chrome steel core (best viewed in color).

$$3 \cos^2 \theta - 1 = 0, \quad (5)$$

which occurs at  $\theta \approx \pm 54.7^\circ$  and  $\theta \approx \pm 125.3^\circ$ . Thus, while MRI distortion should be minimized at these angles, Fig. 2 suggests that an object of finite dimensions must be placed at a sufficient distance from the core to lie in the dark regions between the lobes.

This hypothesis was validated experimentally using a clinical Siemens Skyra 3 T scanner, by acquiring several images of an orange located at different positions ( $r, \theta$ ) relative to a 3.81 cm spherical chrome steel core. The orange was immersed in water and positioned at the boundary of the homogeneous volume of the scanner, while the core was placed at different positions inside this volume. The angle  $\theta$  was varied for two distances (center to center) to the core,  $r = 25$  cm ( $\approx 13R$ ) and  $r = 40$  cm ( $\approx 21R$ ). The imaging sequence used was spin echo for its well-known robustness to field inhomogeneities. Fig. 3 compares the resulting images (coronal plane) with a reference image acquired before inserting the core inside the scanner. Whereas images acquired at  $\theta = 0^\circ$  and  $\theta = 90^\circ$  are significantly altered at  $21R$  and show a complete loss of signal at  $13R$ , images taken around the theoretical optimal angle  $54.7^\circ$  are much more accurate. Although the image acquired at 25 cm at this angle is geometrically distorted, some small details remain visible in the lower distortion region (brighter area). One relevant observation is that, in all these images, the slice selected by the radiofrequency excitation pulse was also vertically distorted due to the non-uniform Larmor frequency. The slices were thus not perfectly horizontal as they should, nor exactly located at the expected vertical position. This is shown by the smaller diameter of the orange slice at  $\theta = 0^\circ$  and  $\theta = 90^\circ$  and by the visible seeds varying across images. However, no pure scaling effects are observable in these experiments. Note that for drug targeting assessment, images need not be perfectly accurate from the anatomical point of view. Some level of alteration is acceptable as long as features can be recognized in order to localize the particles. Moreover, volume images (multiple slices) can be acquired so that the region of interest is covered even if slices are distorted.

These results motivated a navigation experiment using MRI to assess targeting in the presence of a core. The

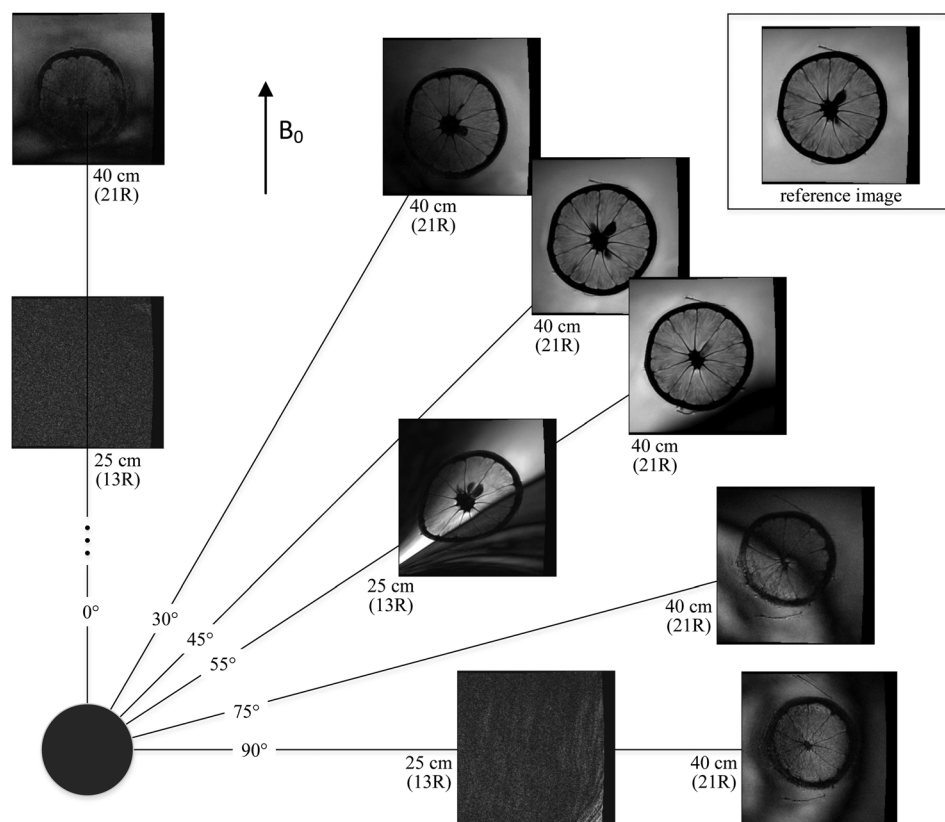


FIG. 3. MR coronal images of an orange, acquired in the presence of a 3.81 cm chrome steel core located at different positions. Imaging parameters: turbo spin echo, TE = 117 ms, TR = 3500 ms, ETL = 19, pixel bandwidth = 260 Hz, slice thickness = 3 mm.

experiment consisted of sequentially navigating particles to two different targets in a vascular phantom. This phantom, which was made of transparent plastic tubes and junctions, had two levels of branching with a constant inner diameter of 1.59 mm. A filter was placed in each of the four output branches to capture the injected particles. The targeted regions were the rightmost branch for the first navigation and the leftmost branch for the second navigation. Both targets required navigating two consecutive bifurcations, separated by 2.5 cm and 3.3 cm, respectively. The phantom was fixed in gelatin to increase the resonance signal for imaging. For the two targeting tasks, a single spherical core (chrome steel, diameter 3.81 cm) was positioned at coordinates  $(-7.3 \text{ cm}, -1.5 \text{ cm})$  and  $(8 \text{ cm}, -1.5 \text{ cm})$ , respectively, relative to the first bifurcation (core's center vertically aligned with the phantom). These locations were selected using an optimization approach.<sup>10</sup> The imaging position of the core was set to  $\theta = 55^\circ$  and  $r = 37 \text{ cm}$  from the center of the phantom. Due to the small gradient duty cycle during imaging, the core can remain stationary without being held at this position. The core was

constrained to a track in the horizontal plane (Fig. 4(a)) and was moved between navigation and imaging positions using the scanner's gradient coils (manual control, pulses of 0.2 s at 10 mT/m in  $x$  and 0.5 s at 12 mT/m in  $z$ ). Figs. 4(b) and 4(c) depict the theoretical particle steering gradients, which are generated by the core, along the desired paths on a schematic of the vascular phantom. The setup was placed in the homogeneous volume of the MRI scanner and oriented such that  $\mathbf{B}_0$  was parallel to the general flow direction. To ensure equal flow at each bifurcation, water was pumped from each of the four output branches using syringes mounted on a Harvard Apparatus PHD 2000 pump. The input flow rate from a reservoir was 20 ml/min (16.8 cm/s). Magnetic particles encapsulating ferrofluid (Ferrotec EMG 700,  $M_{\text{sat}} = 25\,860 \text{ A/m}$ ) with an average diameter of  $300 \mu\text{m}$  were injected individually from the outside of the scanner to avoid their aggregation during their transit towards the phantom. A total of eight particles were injected for each target.

To cope with the vertical distortion of the imaging slices explained above, volume images for the entire thickness of

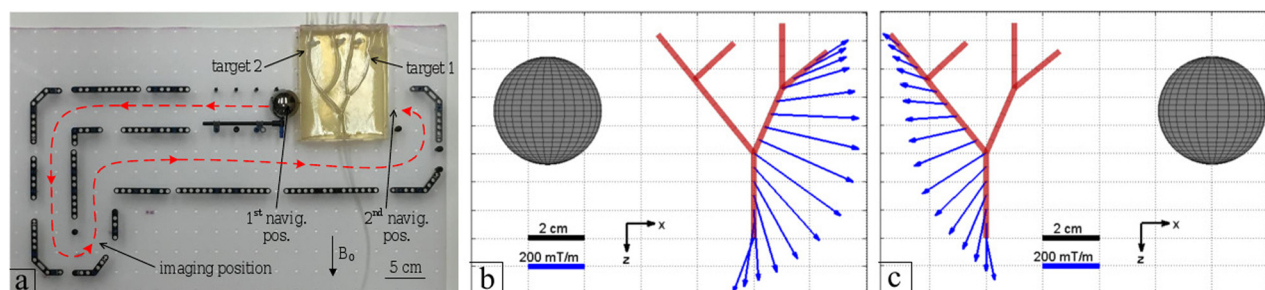


FIG. 4. (a) Experimental setup used for the navigation and imaging experiment. (b) and (c) Optimized core positions (black spheres), for targets 1 and 2, respectively, and theoretical navigation gradients (blue arrows) resulting from the presence of the core along the desired path.



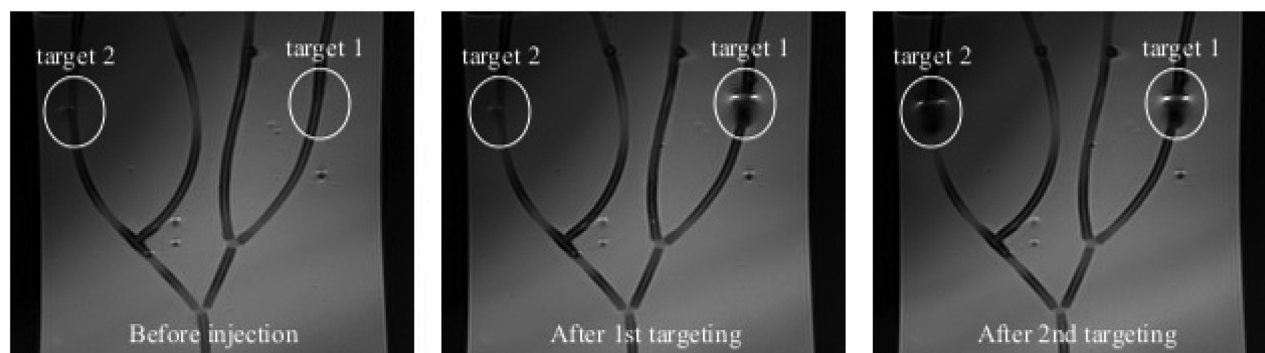


FIG. 5. Coronal images of the phantom resulting from the combination of slice images acquired during the navigation experiment, with the core located at its imaging position. Each image is the result of 5 slice images blended together using transparency gradients in order to cope with slice depth distortions and provide a full view of the branches. Imaging parameters: spin echo, TE = 9.9 ms, TR = 800 ms, pixel bandwidth = 250 Hz, slice thickness = 3 mm, spacing between slices = 3.9 mm.

the phantom were acquired. With the core located at its imaging position, we observed a vertical shift of the slices of about 3–5 mm in the center and up to 1 cm in some corners of the images. This resulted in a portion of the slices being shifted outside the phantom, where air generates no resonance signal. To facilitate visualization, slice images were blended together using transparency gradients so that a full view of the branches was obtained. Fig. 5 shows the resulting images corresponding to before, between, and after the two navigation tasks. The artifacts created by the magnetic particles are clearly visible in images taken after their navigation. From these, we notice that all injected particles reached the targeted locations. For comparison, Fig. 6 shows a top view photograph of the phantom taken after removal from the scanner, where particles are also only visible in the desired branches.

In summary, we have demonstrated that MRI is possible in specific regions around a ferromagnetic core. The location and shape of these regions relative to the core depend on the resonance frequency offset induced by the core. In particular, the offset is minimized at specific angles relative to the central field and decreases with the distance from the core. Although the images acquired in these regions are likely to exhibit some distortion, we have shown that they can suffice for assessing targeting accuracy during DFN interventions. Furthermore, we have demonstrated that core positioning for both targeting and imaging can be performed using the gradient coils of the scanner. This approach enables efficient and automated navigation and delivery assessment at multiple

target locations. While demonstrated here using spin echo, optimizing the imaging sequence used and the imaging parameters could potentially yield better imaging capabilities. For a given sequence, one could potentially calibrate and estimate particle accumulation at a target site from the size of the artifact. Finally, navigating in 3-D vasculatures generally requires multiple cores to generate the navigation gradient patterns needed.<sup>10</sup> Finding (and moving the cores to) proper positions for imaging in this case would be more challenging and will be addressed in future work.

This work was supported by the Fonds de recherche du Québec—Nature et technologies (FRQNT), the Canada Research Chair in Medical Nanorobotics, the U.S. National Science Foundation under Grant No. IIS-1208509, and the Wyss Institute for Biologically Inspired Engineering.

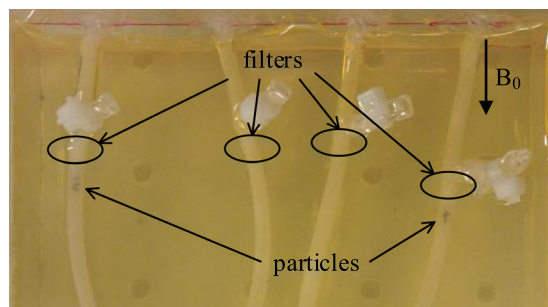


FIG. 6. Postinjection photograph of phantom showing particles in targeted branches. Note that particles shifted away from filters during removal from scanner for photographic imaging.

- <sup>1</sup>P. Vartholomeos, M. Fruchard, A. Ferreira, and C. Mavroidis, “MRI-guided nanorobotic systems for therapeutic and diagnostic applications,” *Annu. Rev. Biomed. Eng.* **13**, 157–184 (2011).
- <sup>2</sup>B. Shapiro, S. Kulkarni, A. Nacev, S. Muro, P. Y. Stepanov, and I. N. Weinberg, “Open challenges in magnetic drug targeting,” *Wiley Interdiscip. Rev.: Nanomed. Nanobiotechnol.* **7**, 446–457 (2015).
- <sup>3</sup>M. Muthana, A. J. Kennerley, R. Hughes, J. Richardson, M. Paul, C. Murdoch, F. Wright, M. Lythgoe, N. Farrow, J. Dobson, J. M. Wild, and C. Lewis, “Directing cell therapy to anatomic target sites in vivo with magnetic resonance targeting,” *Nat. Commun.* **6**, 8009 (2015).
- <sup>4</sup>S. Martel, J.-B. Mathieu, O. Felfoul, A. Chanu, E. Aboussouan, S. Tamaz, P. Pouponneau, L. Yahia, G. Beaudoin, G. Soulez, and M. Mankiewicz, “Automatic navigation of an untethered device in the artery of a living animal using a conventional clinical magnetic resonance imaging system,” *Appl. Phys. Lett.* **90**, 114105 (2007).
- <sup>5</sup>A. Chanu, O. Felfoul, G. Beaudoin, and S. Martel, “Adapting the clinical MRI software environment for real-time navigation of an endovascular untethered ferromagnetic bead for future endovascular interventions,” *Magn. Reson. Med.* **59**, 1287–1297 (2008).
- <sup>6</sup>O. Felfoul, J.-B. Mathieu, G. Beaudoin, and S. Martel, “In vivo MR-tracking based on magnetic signature selective excitation,” *IEEE Trans. Med. Imaging* **27**, 28–35 (2008).
- <sup>7</sup>M. P. Kummer, J. J. Abbott, B. E. Kratochvil, R. Borer, A. Sengul, and B. J. Nelson, “OctoMag: An electromagnetic system for 5-DOF wireless micromanipulation,” *IEEE Trans. Rob.* **26**, 1006 (2010).
- <sup>8</sup>G. Go, H. Choi, S. Jeong, C. Lee, S. Y. Ko, J.-O. Park, and S. Park, “Electromagnetic navigation system using simple coil structure (4 Coils) for 3-D locomotive microrobot,” *IEEE Trans. Magn.* **51**, 1–7 (2015).
- <sup>9</sup>A. Mahmood, M. Dadkhah, M. O. Kim, and J. Yoon, “A novel design of an MPI-based guidance system for simultaneous actuation and monitoring of magnetic nanoparticles,” *IEEE Trans. Magn.* **51**, 1–5 (2015).
- <sup>10</sup>M. Latulippe and S. Martel, “Dipole field navigation: Theory and proof of concept,” *IEEE Trans. Rob.* **31**, 1353–1363 (2015).

- <sup>11</sup>U. Vovk, F. Pernuš, and B. Likar, “A review of methods for correction of intensity inhomogeneity in MRI,” *IEEE Trans. Med. Imaging* **26**, 405–421 (2007).
- <sup>12</sup>W. Lu, K. B. Pauly, G. E. Gold, J. M. Pauly, and B. A. Hargreaves, “SEMAC: Slice encoding for metal artifact correction in MRI,” *Magn. Reson. Med.* **62**, 66–76 (2009).
- <sup>13</sup>M. Carl, K. Koch, and J. Du, “MR imaging near metal with undersampled 3D radial UTE-MAVRIC sequences,” *Magn. Reson. Med.* **69**, 27–36 (2013).
- <sup>14</sup>P. Vartholomeos, C. Bergeles, L. Qin, and P. E. Dupont, “An MRI-powered and controlled actuator technology for tetherless robotic interventions,” *Int. J. Rob. Res.* **32**, 1536–1552 (2013).